Article

Functionalization and Structural Evolution of Conducting Quasi-One-Dimensional Chevrel-Type Telluride Nanocrystals

Kaleolani S. Ogura, Dmitri Leo Mesoza Cordova, Toshihiro Aoki, Griffin M. Milligan, Ze-Fan Yao, and Maxx Q. Arguilla*

Cite This: *Chem. Mater.* 2024, 36, 4714−4725
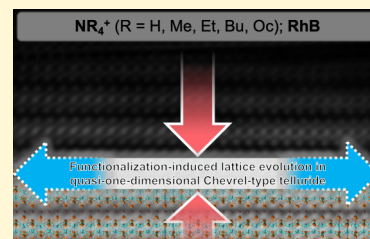
Read Online

ACCESS | Metrics & More | Article Recommendations | SI Supporting Information

ABSTRACT: Interfacing organic molecular groups with well-defined inorganic lattices, especially in low dimensions, enables synthetic routes for the rational manipulation of both their local or extended lattice structures and physical properties. While appreciably studied in two-dimensional systems, the influence of surface organic substituents on many known and emergent one-dimensional (1D) and quasi-1D (q-1D) crystals has remained underexplored. Herein, we demonstrate the surface functionalization of bulk and nanoscale Chevrel-like q-1D ionic crystals using $In_2Mo_6Te_6$, a predicted q-1D Dirac semimetal, as the model phase. Using a series of alkyl ammonium ($-NR_4^+$; R = H, methyl, ethyl, butyl, and octyl) substituents with varying chain lengths, we demonstrate the systematic expansion of the intrachain *c*-axis direction and the contraction of the interchain *a/b*-axis direction with longer chain substituents. Additionally, we demonstrate the systematic expansion of the intrachain *c*-axis direction and the contraction of the interchain *a/b*-axis direction as the alkyl chain substituents become longer using a combination of powder X-ray diffraction and Raman experiments. Beyond the structural modulation that the substituted groups can impose on the lattice, we also found that the substitution of ammonium-based groups on the surface of the nanocrystals resulted in selective suspension in aqueous (NH_4^+-functionalized) or organic solvents (NOc_4^+-functionalized), imparted fluorescent character (Rhodamine B-functionalized), and modulated the electrical conductivity of the nanocrystal ensemble. Altogether, our results underscore the potential of organic−inorganic interfacing strategies to tune the structural and physical properties of rediscovered Chevrel-type q-1D ionic solids and open opportunities for the development of surface-addressable building blocks for hybrid electronic and optoelectronic devices at the nanoscale.

NR_4^+ (R = H, Me, Et, Bu, Oc); **RhB**

Functionalization-induced lattice evolution in quasi-one-dimensional Chevrel-type telluride

1. INTRODUCTION

The creation of hybrid organic−inorganic materials has reliably demonstrated that the interface of organic and inorganic building blocks leads to the discovery of nascent physical properties in the solid state. The rich library of organic functional molecules tethered to a suitable inorganic extended lattice framework has facilitated the creation of materials that impart the unique properties of organic molecules with well-defined optical and electronic states in dense inorganic solids. In recent years, solid-state materials with properties ranging from enhanced photoluminescence (PL) quantum yields,[1] efficient electrocatalysts,[2−4] and highly responsive chemiresistive sensors[5] have been derived from hybrid organic−inorganic structures with varying degrees of porosity, surface-to-volume ratios, and atomic-scale dimensionalities. Owing to the discovery of surface-addressable two-dimensional (2D) ionic and van der Waals (vdW) solids,[6−12] significant advancements have been achieved in the development of hybrid functional materials that approach the atomic scale. In particular, germananes,[13−15] polysilanes,[16,17] and 2D hybrid perovskites[18−20] have garnered immense attention for their modular and surface-addressable states that arise from intrinsic ionic interactions across the layers. The anionic nature of the 2D layers endows these low-dimensional crystalline phases with a facile means toward their functionalization with cationic groups, providing opportunities to tailor their properties and reactivity with the library of organic molecules bearing cationic moieties. The surface modularity in these 2D crystals, coupled with the diverse optical and electronic characters of both the inorganic and organic components, has therefore enabled these hybrid 2D phases to be deployed as building blocks in next-generation electronic and optoelectronic devices.[21−26]

Beyond materials in two dimensions, the search for well-defined solid-state materials with even lower dimensionalities has led to the rediscovery of one-dimensional (1D) crystals with chain-like building blocks, whose cross sections approach the subnanometer regime.[27−34] Of these, 1D crystals that display metallic and semimetallic characteristics have gained recent attention owing to their potential to harness unusual charge density waves, superconductivity, and topologically insulating states. From a materials discovery standpoint, the
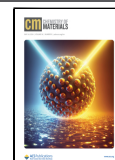
inherent susceptibility of 1D metals and semimetals toward Peierls distortion-induced phase transition hinders the realization and isolation of these phases, especially approaching the atomic scale.[35,36] This renewed interest in solid-state 1D and quasi-1D (q-1D) materials with subnanometer building blocks has motivated recent efforts to understand the structure and physical properties of a family of molybdenum-based Chevrel-like q-1D ionic lattices.[37−42] These q-1D lattices are characterized by anionic metal-chalcogenide (M-Ch) infinite chains that are separated or intercalated by monovalent cations (A) with an $A_2Mo_6Ch_6$ (where A = Li, Na, K, Rb, Cs, In, Tl; Ch = S, Se, Te) stoichiometry. Recent first-principles computational reports,[43] along with early electrical transport measurements[44−48] on this molybdenum-chalcogenide family of q-1D crystals, have shown that the pairing of larger chalcogen atoms (for example, Se, Te) with a sizable monovalent cation (e.g., Rb, Tl, In) results in the suppression of a Peierls distortion-like metal-to-insulator (M-I) structural phase transition. When this M-I transition is suppressed, a rare cubic Dirac Fermionic state along the long-chain, 1D, axis also emerges near the Fermi level.

Experimentally, the Mo family of phases has been shown to exhibit metallic or semiconducting characteristics across a wide temperature or pressure range, which, in some cases, down to freestanding nanowires. For instance, Tl- and In-based analogs of $A_2Mo_6Se_6$ phases have been shown to be superconducting at low temperatures,[45,46] while alkali metal analogs show M-I transitions.[47,48] Additionally, several studies[49−52] have shown that the highly air-sensitive and semiconducting $Li_2Mo_6Se_6$ phase is soluble in aqueous solutions that facilitate the facile substitution of the Li^+ ions by positively charged amine-based organic groups such as octadecylamine, oleylamine, and amine-terminated polystyrene.[53] Leveraging this versatility of cationic functionalization, if applied to ionic 1D metals based on Chevrel-like q-1D chalcogenides, holds promise for diverse applications ranging from fluorescent biosensors[54] to bio-molecule nanosensors.[55] Among these Chevrel-like q-1D phases, one of the compositions that do not bear highly reactive or toxic cations is air-stable and is also predicted to possess this cubic Dirac state is $In_2Mo_6Te_6$. However, because of their less pronounced dispersibility in aqueous solutions, no such studies have been conducted on metallic and non-dispersible $A_2Mo_6Ch_6$ counterparts, such as $In_2Mo_6Te_6$.

In this study, we used $In_2Mo_6Te_6$ as a model phase and showed that both the bulk and nanoscale crystals of the q-1D Chevrel-like telluride-based crystals can be functionalized by cationic organic functional groups ranging from hydrophilic/hydrophobic alkyl groups to fluorescent molecules (Figure 1). First, we describe the synthesis of well-defined bulk crystals of $In_2Mo_6Te_6$ precursors from traditional solid-state melt growth. Using high-angle annular dark-field scanning transmission electron microscopy (HAADF-STEM), we show a direct evidence that points toward long-range, nondimerized periodic ordering of the $[Mo_6Te_6]_n^-$ chains in this phase. Using a series of quaternary ammonium cations in the form of $−NR_4^+$ (R = H, methyl, ethyl, butyl, and octyl) (Figure 1B), we demonstrate that a core−shell-like structure is formed, wherein the organic $(−NR_4^+)_x$ groups are tethered around the inorganic $In_{2−x}Mo_6Te_6$ nanocrystalline core, forming a hybrid $In_2(NR_4)_xMo_6Te_6$ structure. Powder X-ray diffraction and Raman spectroscopic measurements of these hybrid nano-crystalline structures revealed consistent anisotropic modulation in the lattice, which we found to be systematically
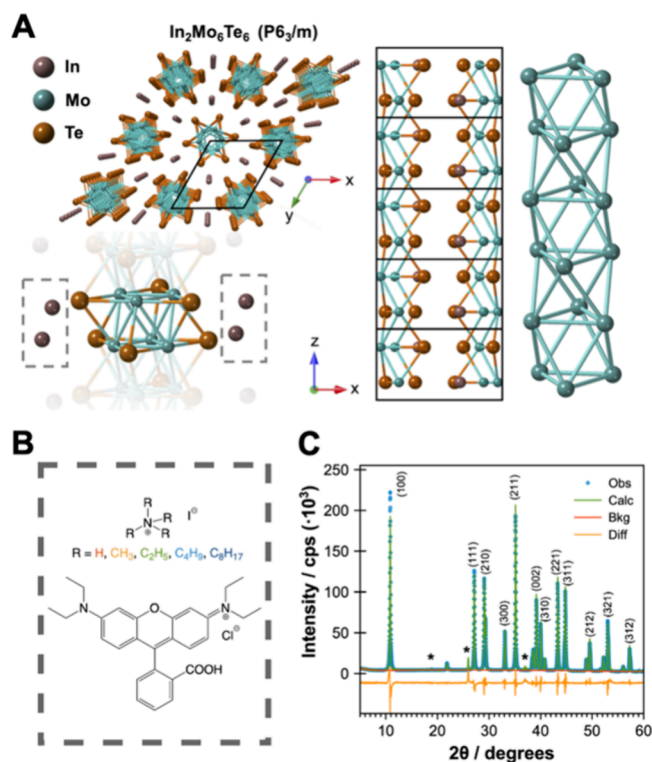

Figure 1. Structural characterization of surface-functionalizable $In_2Mo_6Te_6$ crystals. (A) Crystal structure of $In_2Mo_6Te_6$. The unit cell is characterized by a quarter of a chain occupancy with two cationic positions. (B) Structure of cationic organic functional groups used in this study to substitute In cations on the surface (represented by dashed rectangles in A). (C) Le Bail fitting of the PXRD pattern of the precursor $In_2Mo_6Te_6$ crystals. Asterisks indicate peaks from the minor impurity phase, MoO_3.

related to the size and length of the -R group. Moreover, by leveraging the cationic character of a highly fluorescent dye, such as Rhodamine B (RhB), we also show that RhB can be readily tethered onto the nanocrystal surface with the formation of molecular surface aggregates that display luminescence in the solid state. Finally, we evaluated the electrical transport properties of the resulting hybrid surface-functionalized nanocrystals, which showed a trend in ensemble conductivity as a function of both the alkyl chain length of $−NR_4^+$ and the average grain size within each sample.

2. EXPERIMENTAL SECTION

2.1. Solid-State Synthesis of Bulk $In_2Mo_6Te_6$ Crystals. Elemental precursors of In (99.9%, Strem Chemicals Inc.), Mo (99.5%, Strem Chemicals Inc.), and Te (99.9%, Strem Chemicals Inc.) were used as purchased and were mixed in appropriate stoichiometric ratios and placed in a quartz ampule evacuated to 45 mTorr. The precursors were heated to 1000 and 1050 °C for 2 days and 14 h, respectively,[39,56] and then cooled to room temperature over 3 days in a single-zone vertical tube furnace.

2.2. Liquid-Phase Exfoliation of Bulk $In_2Mo_6Te_6$ Crystals. Powder samples of bulk $In_2Mo_6Te_6$ crystals were placed in a glass vial and dispersed in an optimized volume fraction of isopropanol (*i*-PrOH) to water (50% v/v), with a starting concentration of powder as 1 mg/mL. The suspension was sonicated at room temperature for 1 h and centrifuged at 4500 r.p.m. for 10 min to remove residual precursor powders. The resulting exfoliated nanocrystals were filtered and vacuum-dried.

2.3. Liquid-Phase Functionalization of $In_2Mo_6Te_6$ Nano-crystals into $In_{2−x}(NR_4)_xMo_6Te_6$ (R = H, CH_3, C_2H_5, C_4H_9, and

C_8H_{17}) and $In_{2-x}(RhB)_xMo_6Te_6$. The exfoliated bulk crystals of $In_2Mo_6Te_6$ were suspended in a 50% i-PrOH solution and mixed with 1 mg/mL solution of quaternary ammonium halide or RhB in 50% i-PrOH. The solution was refluxed for 2 days at approximately 80 °C under constant stirring. The functionalized nanocrystals were filtered, washed several times with i-PrOH, and dried for several hours under vacuum. The ammonium halides used as precursors were NR_4I (R = H, CH_3, C_2H_5, and C_4H_9), NR_4Br (R = C_8H_{17}), and RhB. All reagents were obtained from Sigma-Aldrich and had a purity of 99.9%.

2.4. Powder X-Ray Diffraction (PXRD) and Data Fitting. Powder diffractograms were collected using a Rigaku Miniflex 600 diffractometer equipped with a Cu Kα source. All diffractograms were calibrated using LaB_6 (Sigma-Aldrich, 99.9%) as the internal standard. The resulting diffraction patterns were processed by Le Bail fitting and the approximate grain sizes were extracted using the FullProf suite.

2.5. SEM and Energy-Dispersive Spectroscopy. SEM images were collected using a FEI Magellan XHR SEM operated at 30 keV and 0.8 nA. Energy-dispersive spectroscopy (EDS) data were collected with an Oxford 80 mm^2 Silicon Drift Detector (SDD) and analyzed using the Aztec software. Samples for SEM-EDS were prepared by embedding the powder samples onto a carbon tape secured onto aluminum stubs. The samples were then flattened to ensure physical contact.

2.6. Raman and PL Spectroscopy. Raman and PL spectra were collected using a Renishaw InVia system equipped with a charge-coupled device (CCD) detector. The spectra were acquired using 532 and 785 nm lasers with suitable gratings depending on the experimental conditions. A 2400 mm^{-1} grating was used for Raman spectroscopy and a 1200 mm^{-1} grating was used for PL spectroscopy. Raman spectra were recorded at a nominal laser power of 1.028 to 1.09 mW with 5s of exposure time. The PL spectra (532 nm excitation) were taken at a nominal laser power of 0.22 mW with 10 to 20 s exposure time. PL spectral maps (532 nm excitation) were obtained using the Wire 4.4 streamline high-resolution mapping feature at a nominal laser power of 0.0206 mW with an exposure time of 2 s and a 200 nm step size per pixel. PL maps were constructed with integrated peak areas along a 0.05 eV window.

2.7. HAADF-STEM and Elemental Mapping. HAADF-STEM images and subsequent EDS elemental mapping were obtained using an aberration-corrected JEOL Grand ARM 300CF equipped with a dual 100 mm^2 SDD operated at 300 kV. The fast Fourier transform (FFT) of the HAADF-STEM images was created using ImageJ software and indexed with a simulated diffraction pattern of $In_2Mo_6Te_6$ using the SingleCrystal software.

2.8. Transmission Electron Microscopy. $In_{2-x}(NR_4)_xMo_6Te_6$ was aliquoted midway through the reaction of $In_2Mo_6Te_6$ with $N(C_8H_{17})_4Br$ and drop-cast onto a lacey carbon TEM Grid (Ted Pella). Transmission electron microscopy (TEM) images were acquired on JEOL JEM-2800 S/TEM operated at 200 kV.

2.9. Liquid-Phase Fluorescence Spectroscopy. The fluorescence spectra of the RhB solutions were recorded using a Cary Eclipse fluorescence spectrometer equipped with a Xenon flash lamp. The fluorescence emission was measured in the 510−1000 nm range at an excitation wavelength of 500 nm.

2.10. Fluorescence Optical Microscopy. Optical fluorescence images were captured using a Keyence BZ-X800E fluorescence microscope. Images were captured in bright field, phase contrast, and through a red channel fluorescence filter (BZ-X TRITC, excitation at 545 nm and emission at 605 nm). All optical images were processed using Keyence BZ-X800 and ImageJ software.

2.11. Liquid-Phase Ultraviolet−Visible Spectroscopy. The absorbance spectra of the water/hexane-dispersed $In_2Mo_6Te_6$, $In_{2-x}(NH_4)_xMo_6Te_6$, and $In_{2-x}(NOc_4)_xMo_6Te_6$ nanocrystals were taken using an Agilent Cary 100 ultraviolet−visible (UV−vis) spectrophotometer that was scanned in the 280−600 nm range.

2.12. Zeta Potential Measurements of Dispersed Nanocrystals. The Zeta potential of the dispersed nanocrystals was measured using a Malvern Zetasizer ZS Nano DLS. Dried powders of nonfunctionalized and functionalized nanocrystals were dispersed in a 50% v/v i-PrOH:H_2O solvent to yield a suspension with a concentration of ~0.25 mg/mL. This suspension was injected into a DTS1070 disposable folded capillary cell that was subsequently measured in the Malvern Zetasizer ZS Nano DLS system.

2.13. Electrical Transport Measurements of Pelletized Nanocrystals. Powder samples were pelletized using an MSE Pro pneumatic press with a 7 mm die-cast at 7 MPa. The pressed pellets were carefully pasted onto quartz substrates using a thin vacuum grease coat. For the van der Pauw device configuration,[57,58] gold wires (99.9%, 0.025 mm thick, Ted Pella) were placed in contact with the four corners of the pellet, using a silver epoxy mixture (Ted Pella). The other ends of the gold wires were placed in contact with the gold-coated substrates as probe points. The device was mounted onto the sample stage of the Micromanipulator 6000 probe station (Bausch & Lomb). The four probes were placed in contact with each gold substrate, the current was applied through a Keithley 2450 source meter, and conductivity values were measured using the KickStart software.

3. RESULTS AND DISCUSSION

The crystal structure of $In_2Mo_6Te_6$ is characterized by a lattice composed of infinite one-dimensional chains of $[Mo_6Te_6]_n^-$ that run parallel to the crystallographic c-axis and are separated by In cations that act as intercalant species.[37,38] Powders of $In_2Mo_6Te_6$ bulk crystals were prepared via a solid-state melt synthesis route that was modified from the existing literature.[37,39] Le Bail fitting of the PXRD pattern of the resulting bulk crystals was consistent with the previously reported hexagonal P6$_3$/m space group (No. 176) (Figure 1C, Table S1). The fitting process revealed that the products were composed of the target $In_2Mo_6Te_6$ phase with trace amounts of MoO_3 impurities that likely formed from the oxidation of Mo from the TeO_2 species intrinsic to the surface of the Te precursor (Figure S1), similar to what has been observed in literature reports of related phases.[37,56] Elemental mapping of these bulk crystals by EDS confirmed the near-stoichiometric distribution of In:Mo:Te throughout the crystals (Figures 2A and S2; Table S2). Based on these EDS measurements, we note that there was a consistent deficiency of In atoms across several samples. Preliminary EDS analyses on sizable and isolated single crystals of $In_2Mo_6Te_6$ have also shown
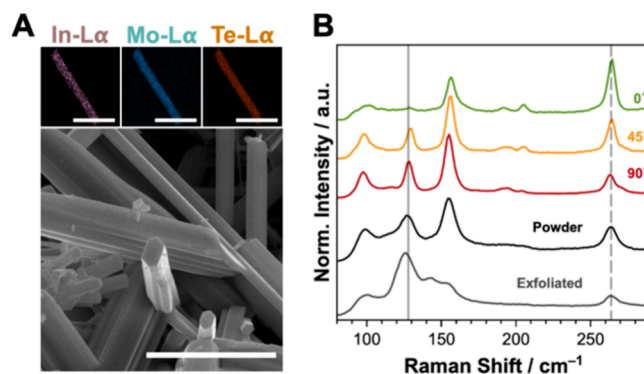

Figure 2. Structural morphology and lattice dynamics of $In_2Mo_6Te_6$ bulk and nanocrystals. (A) Representative SEM and EDS elemental maps of the $In_2Mo_6Te_6$ bulk crystals. Scale bars, 10 μm for SEM and 2.5 μm for EDS. (B) Orientation-dependent Raman spectra of large $In_2Mo_6Te_6$ bulk crystals with polarization of the incident 785 nm laser oriented parallel (green), angled (yellow), and perpendicular (red) with respect to the long axis of the crystal. The ensemble Raman spectra of the powder (black) and exfoliated (gray) polycrystals are also included.
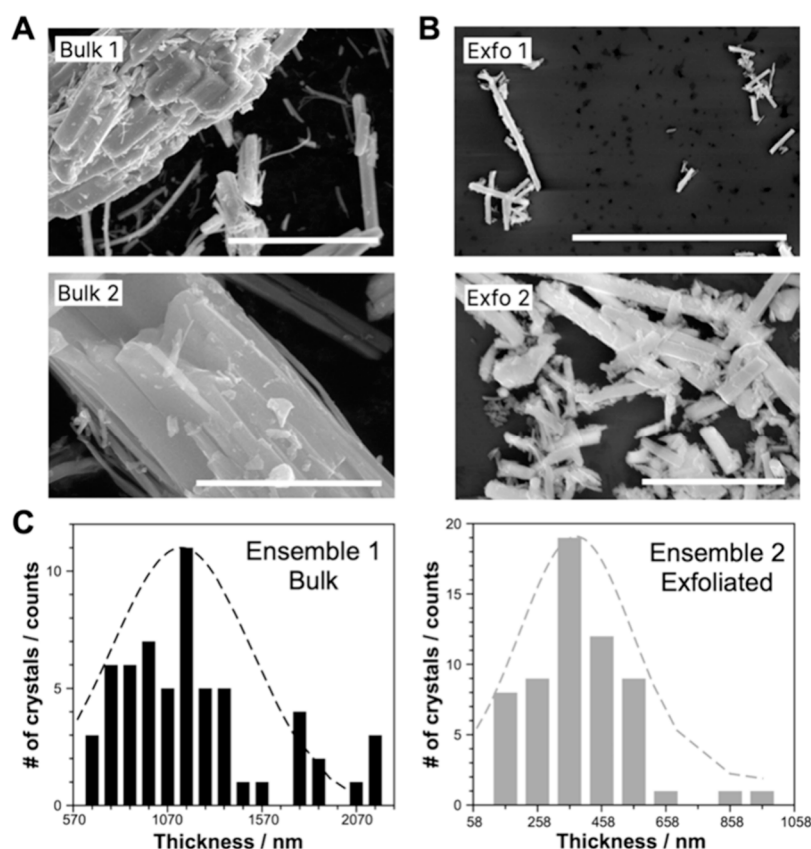
Figure 3. Additional representative SEM images of bulk and exfoliated $In_2Mo_6Te_6$ nanocrystals and statistics. Images of (A) bulk and (B) exfoliated nanocrystals. Scale bars for 1 are 30 μm and 2 are 5 μm. (C) Histograms representing the cross-sectional distributions of as-synthesized bulk polycrystals (left) and liquid-exfoliated (right) nanocrystals of $In_2Mo_6Te_6$. The representative ensemble SEM images are shown in Figure S2. For each plot, each thickness count takes into account a $\pm$ 50 nm thickness range with a normalized distribution curve (dashed curve).

consistent deficiencies of In atoms across several single crystals in the order of ~12% or an average δ of 0.24 in $In_{2-\delta}Mo_6Te_6$ (Table S3). The nature and origin of these In vacancies, which have not been explored in prior reports on this phase, will be the subject of a follow-up study. However, for simplicity and the scope of our study, we refer to this phase as "$In_2Mo_6Te_6$" throughout this report.

SEM images of the needle-like $In_2Mo_6Te_6$ bulk crystals show highly anisotropic crystals bearing hexagonal facets, whose morphologies are consistent with the q-1D crystal habit of the $In_2Mo_6Te_6$ lattice. Higher-magnification SEM images show the fibrous morphology of these crystals, also consistent with the one-dimensional nature of the $[Mo_6Te_6]_n^-$ chains that are bundled in the crystal structure (Figure S3). Although often denoted as ionic lattices, we found that $In_2Mo_6Te_6$ bulk crystals readily unbundle even with mild mechanical agitation, which suggests that there is a weak ionic interaction between the In cation and $[Mo_6Te_6]_n^-$ chains. This observation motivated us to derive nanocrystalline analogs from the bulk using a top−down approach by subjecting the $In_2Mo_6Te_6$ bulk crystals to liquid-phase exfoliation by ultrasonication. In this process, we used a 50% v/v *i*-PrOH:H_2O solvent mixture that we found to most effectively suspend the exfoliated $In_2Mo_6Te_6$ nanocrystals.[59] The zeta potential of this suspended solution was measured to be −29.70 mV, verifying the weak negative charge character of the $[Mo_6Te_6]_n^-$ chains (Figure S4).[60] Upon exfoliation, we compared the representative ensemble SEM images of bulk and exfoliated $In_2Mo_6Te_6$ and found that the 1D fiber-like morphology was preserved upon exfoliation

(Figure 3). We also found an average cross-section of 1206 $\pm$ 393 nm for the bulk crystallites and 388 $\pm$ 158 nm for exfoliated nanocrystals from 60 individual randomly oriented crystals in the representative micrographs. This 3-fold decrease in the thickness of the $In_2Mo_6Te_6$ crystals establishes weak interchain interactions in the structure and suggests the possibility of In cation substitution on the larger surface exposed in the nanocrystals.

We performed Raman spectroscopy on both the ensemble bulk and larger polycrystals of $In_2Mo_6Te_6$ to further confirm the structural identity of the crystals and to probe the lattice dynamics of the anisotropic q-1D crystal structure. Furthermore, we sought to establish the specific phonon modes corresponding to the intrachain (modes parallel to the long-chain axis of the $[Mo_6Te_6]_n^-$ chains) and interchain (modes perpendicular to the long-chain axis of the $[Mo_6Te_6]_n^-$ chains) directions that will be used as an identifier in subsequent analyses of the functionalized nanocrystals. We first performed ensemble Raman spectroscopy measurements of powder and solution-exfoliated samples of $In_2Mo_6Te_6$ crystals using a 785 nm excitation wavelength (Figure 2B). The Raman spectra of these samples exhibited four characteristic Raman peaks at 98, 125, 154, and 263 cm^{-1}. To empirically determine the symmetry of the Raman peaks, orientation-dependent Raman spectroscopy was performed on well-defined large crystals of $In_2Mo_6Te_6$ that we were able to isolate, also using a 785 nm laser excitation. In these measurements, the crystals were oriented at 0° (parallel) and 90° (perpendicular) with respect to the polarization of the incident laser. We compared the

orientation-dependent Raman intensities of $In_2Mo_6Te_6$ to the isostructural reference phase $In_2Mo_6Se_6$, in which the symmetry assignments have been reported in the literature.[61] Raman peaks in the $In_2Mo_6Te_6$ spectrum that had similar orientation-dependent intensity behavior as the Raman peaks in the $In_2Mo_6Se_6$ spectrum were assigned the corresponding $In_2Mo_6Se_6$ phonon mode symmetries. We found that the peak at 125 cm^{-1} (labeled with a solid line) and the peak at 263 cm^{-1} (labeled with a dashed line) are consistent with phonon modes with E- and A-symmetries of the $[Mo_6Te_6]_n^-$ chains, respectively (Figure 2B). In conjunction with the $In_2Mo_6Te_6$ crystal structure, these orthogonal phonon modes can be used to assess the softening or stiffening of the lattice along the intra- and interchain directions.

To further demonstrate the persistence of the $In_2Mo_6Te_6$ crystal structure at the nanoscale, we performed atomic-resolution HAADF-STEM imaging and analysis of solution-exfoliated nanocrystals (Figure 4A, B). The high-magnification
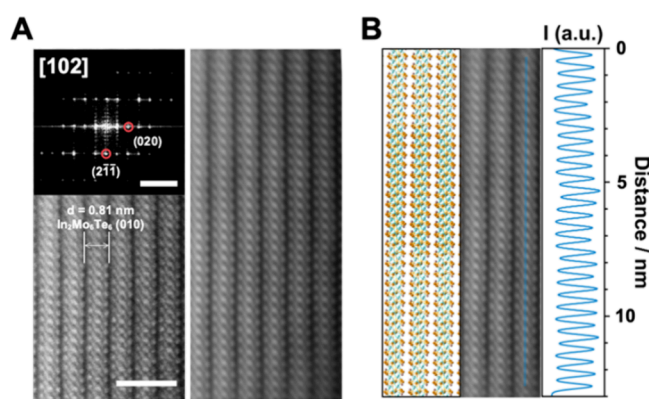

Figure 4. High-magnification STEM images of exfoliated $In_2Mo_6Te_6$ nanocrystals. (A) HAADF-STEM image of an $In_2Mo_6Te_6$ nanocrystal with a raw micrograph (left) and FFT-filtered image (right). The inset shows the FFT image of the [102]-oriented micrograph. Scale bars, 2 nm for image and 0.5 $Å^{-1}$ for FFT. (B) Average intensity plot from the FFT-filtered HAADF-STEM image.

HAADF-STEM image of the bundles of $[Mo_6Te_6]_n^-$ chains in the nanocrystal shows well-ordered bright spots corresponding to Te atoms within the chains (Figure 4A, left). Similarly, the persistent and uniform crystalline order of the atoms along the chain direction can be observed from the FFT-filtered image (Figure 4A, right). As shown in the inset, the extracted local FFT of the micrograph displays distinct intensity spots directly indexed to the [102] zone axis of the $In_2Mo_6Te_6$ crystal structure. We also extracted an intensity profile from the FFT-filtered STEM image to further illustrate the long-range structural order along the chain (Figure 4B). From this profile, the consistently periodic pattern indicates that the atoms that constitute the chains are not disordered, nor Peierls-distorted (dimerized), and are consistent with the unit cell parameter along the c-axis direction of 4.59 Å at room temperature.

The 1D and weakly ionic crystal structure of $In_2Mo_6Te_6$, when exfoliated in solution exposes the In intercalants, opening opportunities for organic functionalization via substitution of surface-exposed In cations as a means to modulate the physical properties of the nanocrystals (Figure 1A, B). Considering that the crystallinity and structural integrity of $In_2Mo_6Te_6$ crystals are well preserved down to the nanoscale, as well as prior reports demonstrating the facile substitution of In ions with

other cationic species,[39,62] $In_2Mo_6Te_6$ is a suitable platform for interfacing q-1D inorganic lattices with cationic organic molecules such as ammonium groups terminated by alkyl chains. To understand the influence of surface cationic organic group substituents on the structure and physical properties of $In_2Mo_6Te_6$, we show that a series of tetra-substituted ammonium salts terminated by either −H or alkane groups of various chain lengths can be appended to the surface of exfoliated $In_2Mo_6Te_6$ nanocrystals (Figure 1B). For this study, bulk powder samples of $In_2Mo_6Te_6$ were exfoliated using a method similar to that described earlier (using a 50% v/v i-$PrOH:H_2O$ solvent mixture) and were combined with solutions of the ammonium salts under study (Figure 1B). The resulting suspension was kept under reflux conditions for 2 days at 80 °C to promote the dissolution of the precursor, especially of ammonium salts that contain long alkane chains, such as NBu_4I or NOc_4Br (see Experimental Section).

We used a combination of PXRD and Raman spectroscopy to characterize the structure of ammonium-functionalized nanocrystals. The powder diffraction patterns of all the samples (Figure 5A) confirmed the preserved general crystallinity and structure of the original precursor material, indicating that the organic groups were primarily on the surface of the nanocrystals.[18−20] The ensemble Raman measurements of
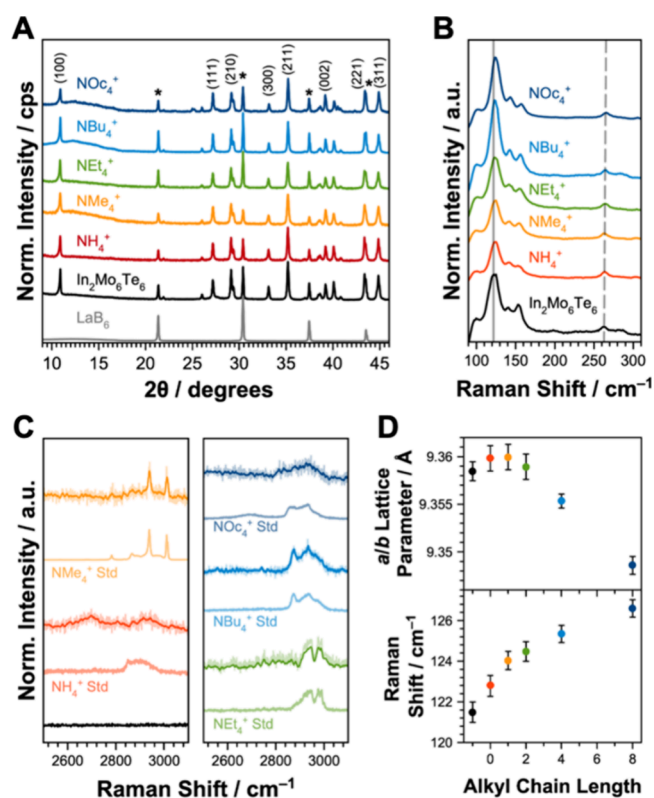

Figure 5. Structural characterization of $In_{2-x}(NR_4)_xMo_6Te_6$ nanocrystals. (A) PXRD and (B) ensemble Raman spectra of the functionalized nanocrystals. (C) High-energy region Raman spectra of the functionalized samples (dark lines) plotted with the corresponding reagent standards of all tertiary ammonium compounds used in the study (light lines). (D) Extracted a-/b-lattice parameters and Raman shifts of $In_{2-x}(NR_4)_xMo_6Te_6$ nanocrystals. The negative alkyl chain length (black) corresponds to the absence of functional groups, and the zero value (red) corresponds to ammonium ions.

the nanocrystals were consistent with the phonon modes observed in the bulk (Figure 5B), suggesting that the lattice of $In_2Mo_6Te_6$ is structurally stable and consistent with our general assessment of the PXRD pattern upon surface functionalization. To confirm the chemical identity of the organic surface functional groups, we performed Raman spectroscopy in the higher energy spectral region of 2500 to 3100 cm^{-1} for each sample to demonstrate that the vibrational stretches of the alkyl ammonium groups on the surface are present in the functionalized $In_{2-x}(NR_4)_xMo_6Te_6$ nanocrystals. All samples showed peaks consistent with the characteristic vibrational stretches of N−H, C−C, N−C, and C−H in the mid-infrared (IR) region (Figure 5C). The broad peaks between 2600 and 3000 cm^{-1} for the $In_{2-x}(NH_4)_xMo_6Te_6$ crystals (red curve) correspond to the overtone modes of N−H.[63−65] The prominent peaks observed for the other functional groups, $-NMe_4^+$ (orange), $-NEt_4^+$ (green), $-NBu_4^+$ (blue), and $-NOc_4^+$ (indigo), can be assigned to the stretching modes of $-CH_3$ groups.[66−69]

We further directly ascertain the successful tethering and uniform coverage of the ammonium groups on the surface of the nanocrystals using HAADF-STEM and EDS analyses of single nanocrystals. From the low-magnification HAADF-STEM image of the representative NOc_4^+-functionalized $In_{2-x}(NR_4)_xMo_6Te_6$ nanocrystals, it is apparent that a carbonaceous amorphous layer is present on the surface of the nanocrystals (Figure 6A). At higher magnifications, we
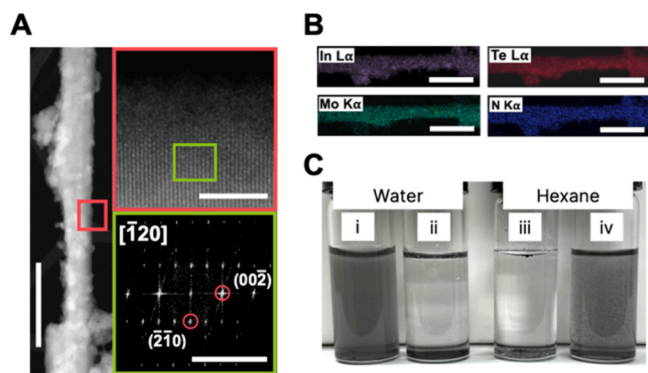

Figure 6. Nanostructure and solution dispersibility of functionalized $In_2Mo_6Te_6$ nanocrystals. (A) Low- (main panel) and high-magnification (red box) HAADF-STEM images of $In_{2-x}(NOc_4)_xMo_6Te_6$ nanocrystals with local FFT (green box) indexed to the [−120] zone axis. Scale bar is 250 nm for low magnification, 5 nm for high magnification, and 100 $Å^{-1}$ for FFT. (B) Corresponding elemental EDS maps of the same nanocrystal shown in (A). Scale bar, 250 nm. (C) Optical images of the nanocrystals of $In_{2-x}(NH_4)_xMo_6Te_6$ (i and iii) and $In_{2-x}(NOc_4)_xMo_6Te_6$ (ii and iv) dispersed in water (left) and hexane (right).

observe that the ordered crystalline core is preserved, which is evidenced by the local FFT showing distinct intensity spots indexed to the [−120] zone axis of $In_2Mo_6Te_6$ (Figure 6A, green box). The elemental composition of the NOc_4^+-functionalized $In_2Mo_6Te_6$ nanocrystal was also mapped using low-magnification EDS, wherein high intensities of the nitrogen-K signal were detected among the stoichiometric precursor elements (Figure 6B). In the control measurements, the nitrogen-K signal was not observed for any of the nonfunctionalized nanocrystals, supporting the presence of ammonium groups on the nanocrystals. It is worth noting that

since the process of exfoliation is stochastic in nature, resulting in nanocrystals that are nonuniform in width (Figure S5). However, the surface functionalization is uniform across the entire surface of the nanocrystal. The intensities of the elemental maps are evenly distributed throughout the nonuniform nanocrystal, indicating a structural feature inherent to the nanocrystal rather than the functionalization process. The nitrogen-K signal is also corroborated by the fact that there are no localized signal intensities on the nanocrystal.

We also observed further unbundling of the nanocrystals during the functionalization step, as evidenced by the splayed-out fiber bundle TEM image of a representative nanocrystal of $In_{2-x}(NOc_4)_xMo_6Te_6$ that we took out midway during the reaction (Figure S6). As a qualitative test and to further demonstrate the influence of the surface functional groups on the properties of the nanocrystals, we independently mixed the NH_4^+- and NOc_4^+-functionalized nanocrystals with deionized (DI) water and hexane. The nanocrystals bearing more polar NH_4^+ groups on the surface were well dispersed in DI water, but not in hexane (Figure 6C; i, ii, respectively). In contrast, the nanocrystals bearing more nonpolar NOc_4^+ groups did not disperse in DI water but were more readily suspended in hexane (Figure 6C; iii, iv, respectively). Additionally, within this dispersion process, the solvent-dependent suspension behavior was verified by UV−vis spectroscopy (Figure S7) and the Zeta potential measurements of the functionalized nanocrystals (Figure S4). We found that the absorbance signal of bare and NH_4^+-functionalized $In_2Mo_6Te_6$ nanocrystals in water was slightly higher than the NOc_4^+-functionalized nanocrystals, indicating the more favorable dispersion in the solvent arising from the more polar character of the surface. On the other hand, the NOc_4^+-functionalized nanocrystals showed a higher absorbance signal in hexane compared to the bare and NH_4^+-functionalized $In_2Mo_6Te_6$ nanocrystals which is to be expected due to its highly nonpolar nature. Furthermore, the zeta potentials of the functionalized nanocrystals were measured to be −9.36 and −7.34 mV for NH_4^+- and NOc_4^+-functionalized nanocrystals, respectively. This qualitatively illustrates that by choosing an appropriate organic functional group, hydrophobicity or hydrophilicity can be imparted to organic-functionalized nanocrystals of $In_2Mo_6Te_6$.

Beyond the imparted surface characteristics of the tethered ammonium groups, we systematically investigated the influence of the surface organic groups on the extended lattice structure of the $In_2Mo_6Te_6$ nanocrystals. We fitted both the diffraction patterns and Raman spectra to extract the a-/b- (interchain direction) and c-lattice (intrachain direction) constants, as well as the corresponding phonon modes with respect to these crystallographic directions. The Le Bail-fitted lattice parameters and Raman shifts are plotted relative to the alkyl chain lengths of the functional groups (Figures 5D and S8−S9; Table S4). Based on the orientation-dependent Raman spectra (Figure 2B), the Raman mode at 125 cm^{-1} is strongly associated with the E-symmetry phonon mode, which primarily is associated with the basal plane direction (interchain direction) of the lattice structure. The extracted Raman shifts for this mode show a pseudolinear increase in energy with increasing alkyl chain length. Generally, we also observed that larger organic groups on the surfaces of the nanocrystals tended to decrease the a-/b-lattice constant, signifying systematic lattice contraction in the crystalline direction perpendicular to the long axis of the nanocrystals.
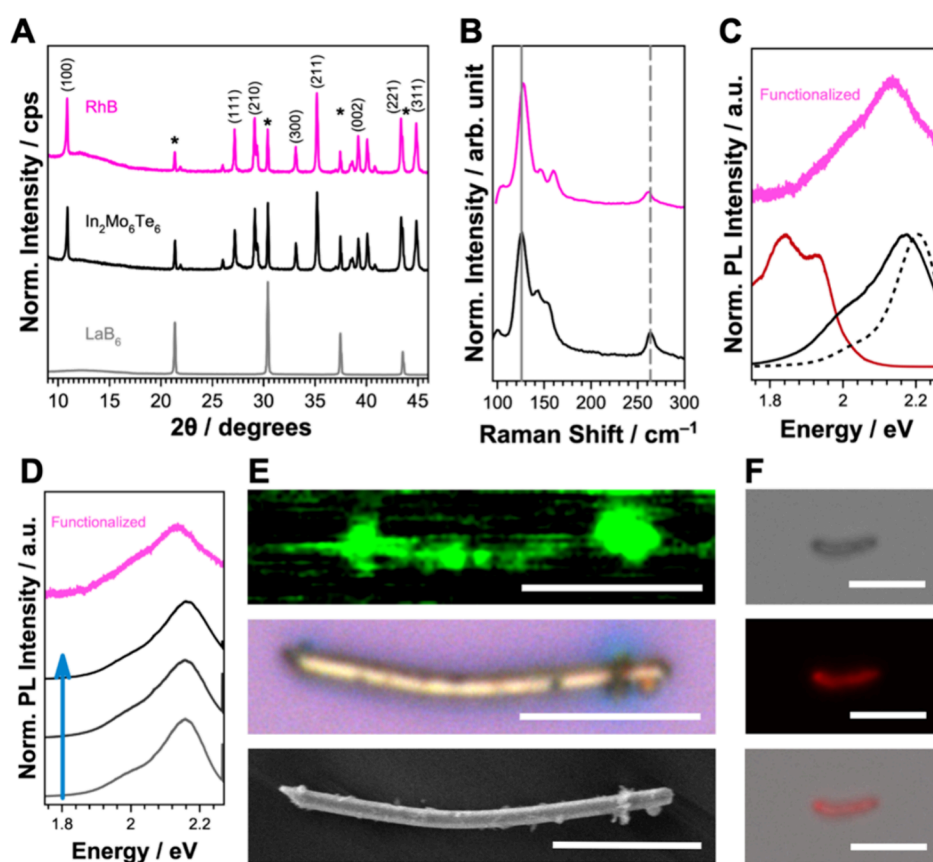
Figure 7. Surface functionalization of $In_2Mo_6Te_6$ nanocrystals with RhB and the resulting optical activity. (A) PXRD and (B) ensemble Raman spectra of $In_{2-x}(RhB)_xMo_6Te_6$ nanocrystals. (C) Emission spectra of RhB-functionalized nanocrystals (magenta) plotted with RhB standards in the form of crystals (red), drop-cast on a Si/SiO_2 substrate (black), and solution (dashed). (D) Concentration-dependent emission spectra of drop-cast RhB on a Si/SiO_2 substrate (black) plotted with RhB-functionalized nanocrystals (magenta). The blue arrow was added as a guide to the eye to indicate the direction of increasing concentration. (E) PL intensity map (top), optical image (middle), and SEM image (bottom) of the RhB-functionalized single crystal. Scale bar, 6.25 μm for PL map and optical, 5 μm for SEM. A 532 nm laser excitation was used for PL spectroscopy and mapping (C−E). (F) Fluorescence microscopy images of the RhB-functionalized single crystal in the BF (top), fluorescence (middle), and overlaid image (bottom). For the fluorescence microscopy experiments, excitation at 545 nm and emission at 605 nm were used. Scale bar, 25 μm.

Considering that both the phonon mode and *a*-/*b*-lattice parameters monotonically evolved with the alkyl ammonium chain length, the longer and larger functional groups (such as $-C_2H_5$, $-C_4H_9$, and $-C_8H_{17}$) are susceptible to intrachain interactions on the surface owing to strong vdW forces across these units; whereas the shorter and smaller groups, such as $-H$ and $-CH_3$, lack these strong attractive forces. From these interactions, along with the HAADF-STEM and EDS mapping (Figure 6A, B), we can consider the hybrid nanocrystal as a structure comprising an organic shell-like aggregate formed around the nanocrystal core, which can range in rigidity depending on the strength of the vdW interactions across the tethered groups on the surface. From this, we infer that, in the case of NH_4^+, the shell around the nanocrystal is less rigid and less sterically crowded, allowing the core lattice of the nanocrystal to remain relatively unperturbed. In contrast, in the case of NOc_4^+, the shell around the nanocrystal is more rigid from the large range of intermolecular vdW interactions and more sterically crowded, resulting in an overall lattice contraction in the *a*-/*b*-direction.[70] The tethering of sizable organic groups on the surface of the nanocrystals can be thought of as an applied chemical pressure on the lattice, resulting in an induced lattice "strain" that is manifested in the stiffening of the Raman modes corresponding to the phonon modes with E-symmetry and the contraction of the lattice in

the *a*/*b*-direction, both of which correspond to the interchain direction. An identical but opposite trend was observed for the A-symmetry phonon mode at 263 cm^{-1} and the *c*-lattice parameter, both of which correspond to the intrachain direction of the crystal (Figure S9). This expected orthogonal trend is consistent with our expectation that the q-1D nature of the lattice can compensate for anisotropic expansion/ contraction across the various axes in the crystal. We anticipate that this anisotropic lattice modulation induced by surface alkyl ammonium substitution could also impose an atomic-level anisotropy in the local coordination environment of Mo that comprise the $[Mo_6Te_6]_n^-$ chains, as was comprehensively reported in Mo-based Chevrel clusters,[71] albeit less pronounced. Probing this, however, would require either high-resolution diffraction techniques or a detailed X-ray absorption spectroscopy analysis which are beyond the scope of this current study.

Beyond the systematic modulation of the nanocrystalline lattice, the ability to readily substitute the surface cations in $In_2Mo_6Te_6$ also enabled the incorporation of functional organic groups that impart optical activity to metallic nanocrystals. To achieve this, exfoliated nanocrystals of $In_2Mo_6Te_6$ were refluxed with a solution of fluorescent RhB dye bearing an ammonium moiety. Similar to tertiary ammonium functionalization, the resulting RhB-functionalized

nanocrystals were characterized by PXRD and Raman spectroscopy (Figure 7A, B). We also found that the diffraction pattern showed the preservation of the crystalline order identical to the original precursor structure. After Le Bail fitting, the lattice parameters extracted from the diffractogram (Table S5) were consistent with the general trends observed in tertiary ammonium-functionalized nanocrystals. Furthermore, the directionally correlated Raman modes at 125 and 263 cm^{-1} shift in directions identical to those of the ammonium groups, in which the E mode shifts to a higher energy and the A mode shifts to a lower energy compared to the pristine $In_2Mo_6Te_6$ crystal.

We probed the visible range emission region of the spectra derived from micro-Raman spectroscopy measurements of the RhB-functionalized nanocrystals to investigate the successful tethering of dye molecules onto the surfaces of $In_2Mo_6Te_6$. Using a 532 nm excitation laser, an intense PL emission signature from the RhB-functionalized nanocrystals was detected around 1.9 to 2.1 eV, which is consistent with the expected fluorescence of the RhB dye (Figure 7C). As a control, we also measured the PL emission of solid-state crystals (plotted in red) and solution drop-casted (plotted in black) standards of RhB, both of which showed a broad emission peak. Additionally, we measured the fluorescence emission spectra of the RhB solution (plotted as a dashed curve), which was found to be similar to that of the drop-casted RhB species. The primary and more intense peak in the high-energy region is commonly assigned to the monomeric form of RhB, while the secondary shoulder peak is assigned to the dimeric form of RhB.[72−74] Consistent with the literature, we found in the spectra of the standard drop-casted RhB samples on Si/SiO_2 (continuous black curve, Figure 7C) that the intensity of the dimer peaks grew and all peaks red-shifted relative to the solution-phase fluorescence spectra of RhB (dashed black curve, Figure 7C). As we expected, this is mainly due to the aggregation of the molecules to form dimers with increasing concentrations.[75,76] Comparing these drop-casted RhB samples on Si/SiO_2 with the freestanding crystals of RhB (red curve, Figure 7C), our results are consistent with the expected significant red shifting of the freestanding crystals, which are highly ordered and predominantly dimerized in contrast to the less-ordered and more polydispersed aggregates of the drop-casted RhB samples.[77]

We measured the concentration-dependent PL spectra of the drop-cast samples from the standard RhB solutions to further assess the relative amounts of RhB species on the surface of the nanocrystals (Figure 7D). We prepared standard RhB solutions of 0.1, 0.4, 1.6, and 6.3 μM, which were drop-casted onto Si/SiO_2 substrates. From the PL measurements of these drop-cast standards, we extracted the peak positions and intensities, which showed a consistent red shift as the concentration of RhB increased for both the monomer and dimer peaks (Figures S10 and S11). Based on these PL spectra, we quantified the propensity for aggregation of the RhB dyes by calculating the intensity ratio of the monomer to dimer (I_M/I_D) PL peaks and plotting them with respect to the RhB solution concentration (Table S6, Figure S12). From this plot, a power regression function of $y = 2.0791x^{-0.095}$ with $R^2 = 0.9648$ was fitted, where x is the estimated concentration of RhB on the surface of the substrate, and y is the PL intensity ratio. Using this regression function, the concentration of the RhB molecules tethered on the surface of the $In_2Mo_6Te_6$ nanocrystals can be approximated to be commensurate to a

drop-casted 0.022 μM (1.1×10^{-5} g L^{-1}) solution of RhB (Table S7), which, as expected, was significantly less dense than compared to the 1.0×10^5 μM (50 g L^{-1}) hypothetical "concentration" extrapolated for the pure RhB crystals. We refer to the "hypothetical concentration" to denote the packing concentration of RhB molecules in an RhB crystal. This significantly lower concentration is to be expected since the surface area of the $In_2Mo_6Te_6$ nanocrystals is much smaller relative to the dense single crystal of RhB, resulting in a significantly more dilute apparent concentration of RhB on the surface of the nanocrystals.

Owing to the imparted optical activity on the $In_2Mo_6Te_6$ nanocrystals, we used optical and electron microscopy techniques to qualitatively characterize and visualize the RhB-functionalized nanocrystals. PL mapping of an RhB-functionalized microcrystallite was performed using laser excitation that closely matched the maximum absorption of RhB (532 nm laser), which was rastered along the surface of the crystal. The PL map showed a pronounced emission intensity on the surface of the nanocrystal (Figure 7E, top). The corresponding optical (Figure 7E, middle) and SEM (Figure 7E, bottom) images of the selected nanocrystal confirm the uniform morphology and preserved crystalline domain of the RhB-functionalized nanocrystals. Complementarily, we probed a freestanding nanocrystal using a fluorescence microscope, wherein the different image channels showed a uniform distribution of RhB chromophores on the surface of the nanocrystal (Figure 7F). These nanocrystals were copiously washed several times with *i*-PrOH to ensure that the emission that we observed arose from the RhB molecules that were strongly tethered onto the surface of the nanocrystal. We performed an identical washing treatment on the drop-cast RhB standard substrates, which resulted in the absence of any PL emission signal observed during the measurement. This further verifies the strong electrostatic attraction of the RhB molecules on the surfaces of the nanocrystals.

Finally, we used the nanocrystalline platform that we developed to study the influence of varying the lengths of the appended surface functional groups on the ensemble electrical conductivity of surface-functionalized $In_2Mo_6Te_6$ (Figure 8). The ensemble electrical transport properties of the functionalized nanocrystals were measured using pressed pellets of each sample. The pelletized samples were imaged using SEM to measure the general surface morphology, which showed well-dispersed and uniform nanocrystals with pronounced grain boundaries (Figure S13). Owing to the high intrinsic conductivity of the metallic $In_2Mo_6Te_6$ phase, the room-temperature electrical conductivities of the pellets were measured using the van der Pauw configuration (Figure 8A, inset) in the dark with conductivities of 171 S cm^{-1} for bulk $In_2Mo_6Te_6$ and 33.3 S cm^{-1} for exfoliated, non-functionalized, $In_2Mo_6Te_6$ nanocrystals (Figure 8B). Relative to the bulk, the overall conductivities of the functionalized pellets were lower and similar to those of exfoliated pellets, which is to be expected given the smaller crystalline domain sizes induced by the exfoliation process (Table S8). These sets of conductivities are comparable to prototypical hybrid polycrystals that are electrically conducting.[78]

The electrical conductivities of the pressed pellets of the functionalized nanocrystalline samples showed a slight increase for small functional groups (for example, NH_4^+- and NMe_4^+-functionalized), whereas nanocrystals bearing larger functional
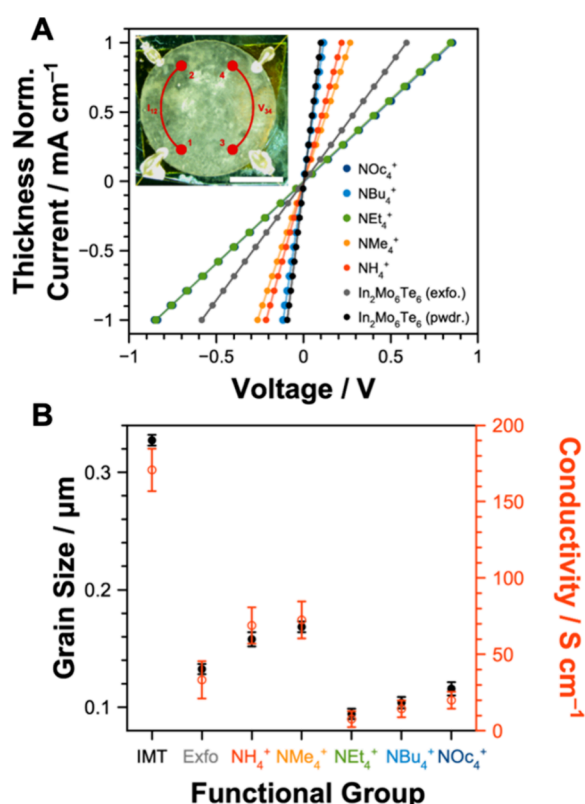
Figure 8. Electrical transport measurements of the pelletized $In_{2-x}(NR_4)_xMo_6Te_6$ nanocrystals. (A) Thickness-normalized current vs voltage curve. The inset shows a representative image of the device fabricated in the van der Pauw configuration. Scale bar, 4 mm. (B) Extracted grain sizes of each sample from the PXRD pattern (left axis) and the measured conductivity values of the functionalized nanocrystals (right axis).

groups displayed decreased conductivity values. In polycrystalline ensembles of hybrid nanocrystals, there are two possible contributors to overall electrical conductivity. First, it can be influenced by the interfacial nature of the domains, that is, the insulating or conducting nature of the surface. Second, it can be influenced by the crystalline domain size of the constituent nanocrystals. By functionalizing the surfaces of these nanocrystals with longer and bulkier alkyl groups, transport along the interchain direction is suppressed due to the insulating nature of the substituent chains, which is consistent with the trend that we observed (Figure 8B). As established in conductive polymer thin films[79−81] and polycrystalline samples,[82] the grain size can also be directly correlated to the electrical conductivity of the sample, wherein larger conductivity values are expected for ensemble samples comprising polycrystals with larger grain sizes. Therefore, we extracted the approximate grain sizes within each sample by fitting the PXRD pattern (Figure 8B). Our results showed larger (smaller) grain sizes for nanocrystals terminated by smaller (bulkier) functional groups, suggesting that the character of the surface functional groups also influences the stabilization of the suspended nanocrystals during synthesis. These trends in the nanocrystalline domain sizes were also consistent with the observed electrical conductivity values, wherein samples with larger grain sizes resulted in larger conductivities and *vice versa*. From these results, we infer that the electrical transport behavior of organic-functionalized

$In_2Mo_6Te_6$ nanocrystals is largely influenced by both the nature of the surface and the crystalline domain size.

4. CONCLUSIONS

In summary, our study demonstrated the successful functionalization of both bulk and nanoscale crystals of $In_2Mo_6Te_6$ with a series of cationic organic functional groups. By employing various hydrophilic/hydrophobic alkyl ammonium groups and a cationic dye molecule, we achieved a hybrid core−shell-like nanocrystalline structure that retained the general crystalline order and symmetry of the precursor crystal. We showed that the surface functionalization of exfoliated $In_2Mo_6Te_6$ nanocrystals can systematically modulate the extended lattice crystal structure, impart nonintrinsic surface characteristics (hydrophilicity, hydrophobicity, and fluorescence), influence the nanocrystalline domain sizes, and tune the ensemble electrical conductivities. Altogether, our results provide opportunities for facile surface functionalization of a sizable class of q-1D Chevrel-like crystals that are not generally soluble in aqueous solutions. We envision that controlled organic functionalization of surfaces that bear an underlying 1D order could lead to next-generation device building blocks that leverage the enhanced physical properties arising from well-ordered and low-dimensional organic substituents.

■ ASSOCIATED CONTENT

Data Availability Statement

All data are available in the main text or the Supporting Information.

Ⓢ Supporting Information

The Supporting Information is available free of charge at https://pubs.acs.org/doi/10.1021/acs.chemmater.4c00468.

> Supplementary data and results: (Figure S1) Powder XRD of Mo and Te precursors; (Figure S2) elemental analyses of representative $In_2Mo_6Te_6$ crystal ensembles using SEM-EDS; (Figure S3) representative SEM images of fiber-like $In_2Mo_6Te_6$ crystals; (Figure S4) zeta potential plot of dispersed nanocrystals; (Figure S5) low-magnification HAADF-STEM of $In_2Mo_6Te_6$ nanocrystal; (Figure S6) low-magnification TEM of $In_{2-x}(NOc_4)_xMo_6Te_6$ nanocrystal; (Figure S7) UV−vis spectra of $In_2Mo_6Te_6$, $In_{2-x}(NH_4)_xMo_6Te_6$, and $In_{2-x}(NOc_4)_xMo_6Te_6$ nanocrystals; (Figure S8) Le Bail-fitted diffractograms of functionalized $In_2Mo_6Te_6$ nanocrystals; (Figure S8) lattice dynamics and parameters of functionalized nanocrystals in the c-axis direction; (Figure S10) example fit of PL emission curve of drop-casted 0.1 μM RhB; (Figure S11) concentration-dependent PL peak energies of drop-casted RhB standards used in this study; (Figure S12) plot of the intensity ratios from Table S6 against different concentrations of RhB solutions drop-casted onto Si/SiO₂ substrates; (Figure S13) representative SEM images of regions sampled from pressed pellets of functionalized and nonfunctionalized $In_2Mo_6Te_6$ used for electrical transport measurements; (Table S1) lattice parameters determined using Le Bail fitting from the diffractogram in Figure 1C; (Table S2) atomic composition of $In_2Mo_6Te_6$ ensemble in Figure S2; (Table S3) preliminary atomic composition of $In_{2-δ}Mo_6Te_6$ single crystals; (Table S4) lattice parameters of the exfoliated and functionalized nanocrystals of

$In_2Mo_6Te_6$ determined by Le Bail fitting of the diffractograms in Figure S9A-F; (Table S5) lattice parameters of RhB-functionalized nanocrystals of $In_2Mo_6Te_6$ determined by Le Bail fitting of the diffractogram in Figure S9G; (Table S6) PL emission peak intensities of drop-casted RhB; (Table S7) PL emission peak of standard and functionalized samples; and (Table S8) extracted conductivity values of each pressed pellet based on electrical transport measurements using the van der Pauw device geometry (PDF)

■ AUTHOR INFORMATION

Corresponding Author

Maxx Q. Arguilla — *Department of Chemistry, University of California Irvine, Irvine, California 92697, United States;* ⊙ orcid.org/0000-0001-9948-0814; Email: marguill@uci.edu

Authors

Kaleolani S. Ogura — *Department of Chemistry, University of California Irvine, Irvine, California 92697, United States*

Dmitri Leo Mesoza Cordova — *Department of Chemistry, University of California Irvine, Irvine, California 92697, United States;* ⊙ orcid.org/0000-0002-7527-8950

Toshihiro Aoki — *Irvine Materials Research Institute, University of California Irvine, Irvine, California 92697, United States;* ⊙ orcid.org/0000-0001-6620-9390

Griffin M. Milligan — *Department of Chemistry, University of California Irvine, Irvine, California 92697, United States;* ⊙ orcid.org/0000-0002-6632-8004

Ze-Fan Yao — *Department of Chemical and Biomolecular Engineering, University of California Irvine, Irvine, California 92697, United States;* ⊙ orcid.org/0000-0001-5590-0768

Complete contact information is available at:
https://pubs.acs.org/10.1021/acs.chemmater.4c00468

Author Contributions

K.S.O.: Methodology, investigation, visualization, writing—original draft preparation and editing; **D.L.M.C.**: Methodology, investigation, writing—reviewing and editing; **T.A.**: Investigation; **G.M.M.**: Investigation; **Z.-F.Y.**: Investigation; **M.Q.A.**: Conceptualization, supervision, writing—reviewing and editing.

Notes

The authors declare no competing financial interest.

■ REFERENCES

(1) Yokota, T.; Kajitani, T.; Shidachi, R.; Tokuhara, T.; Kaltenbrunner, M.; Shoji, Y.; Ishiwari, F.; Sekitani, T.; Fukushima, T.; Someya, T. A Few-Layer Molecular Film on Polymer Substrates to Enhance the Performance of Organic Devices. *Nat. Nanotechnol.* **2018**, *13* (2), 139−144.

(2) Zhao, S.; Wang, Y.; Dong, J.; He, C.-T.; Yin, H.; An, P.; Zhao, K.; Zhang, X.; Gao, C.; Zhang, L.; Lv, J.; Wang, J.; Zhang, J.; Khattak, A. M.; Khan, N. A.; Wei, Z.; Zhang, J.; Liu, S.; Zhao, H.; Tang, Z. Ultrathin Metal−Organic Framework Nanosheets for Electrocatalytic Oxygen Evolution. *Nat. Energy* **2016**, *1* (12), No. 16184.

(3) Clough, A. J.; Yoo, J. W.; Mecklenburg, M. H.; Marinescu, S. C. Two-Dimensional Metal−Organic Surfaces for Efficient Hydrogen Evolution from Water. *J. Am. Chem. Soc.* **2015**, *137* (1), 118−121.

(4) Miner, E. M.; Fukushima, T.; Sheberla, D.; Sun, L.; Surendranath, Y.; Dincă, M. Electrochemical Oxygen Reduction Catalysed by Ni_3(Hexaiminotriphenylene)$_2$. *Nat. Commun.* **2016**, *7* (1), No. 10942.

(5) Campbell, M. G.; Liu, S. F.; Swager, T. M.; Dincă, M. Chemiresistive Sensor Arrays from Conductive 2D Metal−Organic Frameworks. *J. Am. Chem. Soc.* **2015**, *137* (43), 13780−13783.

(6) Xue, J.; Sanchez-yamagishi, J.; Bulmash, D.; Jacquod, P.; Deshpande, A.; Watanabe, K.; Taniguchi, T.; Jarillo-herrero, P.; Leroy, B. J. Scanning Tunnelling Microscopy and Spectroscopy of Ultra-Flat Graphene on Hexagonal Boron Nitride. *Nat. Mater.* **2011**, *10* (4), 282−285.

(7) Yan, Z.; Sun, Z.; Lu, W.; Yao, J.; Zhu, Y.; Tour, J. M. Controlled Modulation of Electronic Properties of Graphene by Self-Assembled Monolayers on SiO_2 Substrates. *ACS Nano* **2011**, *5* (2), 1535−1540.

(8) Schaibley, J. R.; Yu, H.; Clark, G.; Rivera, P.; Ross, J. S.; Seyler, K. L.; Yao, W.; Xu, X. Valleytronics in 2D Materials. *Nat. Rev. Mater.* **2016**, *1* (11), No. 16055.

(9) Mannix, A. J.; Kiraly, B.; Hersam, M. C.; Guisinger, N. P. Synthesis and Chemistry of Elemental 2D Materials. *Nat. Rev. Chem.* **2017**, *1* (2), No. 0014.

(10) Bhimanapati, G. R.; Lin, Z.; Meunier, V.; Jung, Y.; Cha, J.; Das, S.; Xiao, D.; Son, Y.; Strano, M. S.; Cooper, V. R.; Liang, L.; Louie, S. G.; Ringe, E.; Zhou, W.; Kim, S. S.; Naik, R. R.; Sumpter, B. G.; Terrones, H.; Xia, F.; Wang, Y.; Zhu, J.; Akinwande, D.; Alem, N.; Schuller, J. A.; Schaak, R. E.; Terrones, M.; Robinson, J. A. Recent Advances in Two-Dimensional Materials beyond Graphene. *ACS Nano* **2015**, *9* (12), 11509−11539.

(11) He, S.; Evans, A. M.; Meirzadeh, E.; Han, S. Y.; Russell, J. C.; Wiscons, R. A.; Bartholomew, A. K.; Reed, D. A.; Zangiabadi, A.; Steigerwald, M. L.; Nuckolls, C.; Roy, X. Site-Selective Surface Modification of 2D Superatomic Re_6Se_8. *J. Am. Chem. Soc.* **2022**, *144* (1), 74−79.

(12) Choi, B.; Lee, K.; Voevodin, A.; Wang, J.; Steigerwald, M. L.; Batail, P.; Zhu, X.; Roy, X. Two-Dimensional Hierarchical Semiconductor with Addressable Surfaces. *J. Am. Chem. Soc.* **2018**, *140* (30), 9369−9373.

(13) Knapp, D.; Brunschwig, B. S.; Lewis, N. S. Chemical, Electronic, and Electrical Properties of Alkylated Ge(111) Surfaces. *J. Phys. Chem. C* **2010**, *114* (28), 12300−12307.

(14) Buriak, J. M. Organometallic Chemistry on Silicon and Germanium Surfaces. *Chem. Rev.* **2002**, *102* (5), 1271−1308.

(15) He, J.; Lu, Z.-H.; Mitchell, S. A.; Wayner, D. D. M. Self-Assembly of Alkyl Monolayers on Ge(111). *J. Am. Chem. Soc.* **1998**, *120* (11), 2660−2661.

(16) Okamoto, H.; Kumai, Y.; Sugiyama, Y.; Mitsuoka, T.; Nakanishi, K.; Ohta, T.; Nozaki, H.; Yamaguchi, S.; Shirai, S.; Nakano, H. Silicon Nanosheets and Their Self-Assembled Regular Stacking Structure. *J. Am. Chem. Soc.* **2010**, *132* (8), 2710−2718.

(17) Dahn, J. R.; Way, B. M.; Fuller, E.; Tse, J. S. Structure of Siloxene and Layered Polysilane (Si_6H_6). *Phys. Rev. B* **1993**, *48* (24), 17872.

(18) Wang, C.; Yang, S.; Chen, X.; Wen, T.; Yang, H. G. Surface-Functionalized Perovskite Films for Stable Photoelectrochemical Water Splitting. *J. Mater. Chem. A* **2017**, *5* (3), 910−913.

(19) Baikie, T.; Fang, Y.; Kadro, J. M.; Schreyer, M.; Wei, F.; Mhaisalkar, S. G.; Graetzel, M.; White, T. J. Synthesis and Crystal Chemistry of the Hybrid Perovskite (CH_3NH_3)PbI_3 for Solid-State

Sensitized Solar Cell Applications. *J. Mater. Chem. A* **2013**, *1* (18), 5628.

(20) Yang, S.; Wang, Y.; Liu, P.; Cheng, Y.-B.; Zhao, H. J.; Yang, H. G. Functionalization of Perovskite Thin Films with Moisture-Tolerant Molecules. *Nat. Energy* **2016**, *1* (2), No. 15016.

(21) Madhushankar, B. N.; Kaverzin, A.; Giousis, T.; Potsi, G.; Gournis, D.; Rudolf, P.; Blake, G. R.; Van der wal, C. H.; Van wees, B. J. Electronic Properties of Germanane Field-Effect Transistors. *2D Mater.* **2017**, *4* (2), No. 021009.

(22) Amamou, W.; Odenthal, P. M.; Bushong, E. J.; O'hara, D. J.; Luo, Y. K.; Van baren, J.; Pinchuk, I.; Wu, Y.; Ahmed, A. S.; Katoch, J.; Bockrath, M. W.; Tom, H. W. K.; Goldberger, J. E.; Kawakami, R. K. Large Area Epitaxial Germanane for Electronic Devices. *2D Mater.* **2015**, *2* (3), No. 035012.

(23) Lei, Y.; Chen, Y.; Zhang, R.; Li, Y.; Yan, Q.; Lee, S.; Yu, Y.; Tsai, H.; Choi, W.; Wang, K.; Luo, Y.; Gu, Y.; Zheng, X.; Wang, C.; Wang, C.; Hu, H.; Li, Y.; Qi, B.; Lin, M.; Zhang, Z.; Dayeh, S. A.; Pharr, M.; Fenning, D. P.; Lo, Y. H.; Luo, J.; Yang, K.; Yoo, J.; Nie, W.; Xu, S. A Fabrication Process for Flexible Single-Crystal Perovskite Devices. *Nature* **2020**, *583* (7818), 790−795.

(24) Heo, J. H.; Im, S. H.; Noh, J. H.; Mandal, T. N.; Lim, C. S.; Chang, J. A.; Lee, Y. H.; Kim, H. J.; Sarkar, A.; Nazeeruddin, M. K.; Grätzel, M.; Seok, S. Il. Efficient Inorganic-Organic Hybrid Heterojunction Solar Cells Containing Perovskite Compound and Polymeric Hole Conductors. *Nat. Photonics* **2013**, *7* (6), 486−491.

(25) Yu, W.; Li, F.; Yu, L.; Niazi, M. R.; Zou, Y.; Corzo, D.; Basu, A.; Ma, C.; Dey, S.; Tietze, M. L.; Buttner, U.; Wang, X.; Wang, Z.; Hedhili, M. N.; Guo, C.; Wu, T.; Amassian, A. Single Crystal Hybrid Perovskite Field-Effect Transistors. *Nat. Commun.* **2018**, *9* (1), 5354.

(26) Kim, Y. H.; Zhai, Y.; Lu, H.; Pan, X.; Xiao, C.; Gaulding, E. A.; Harvey, S. P.; Berry, J. J.; Vardeny, Z. V.; Luther, J. M.; Beard, M. C. Chiral-Induced Spin Selectivity Enables a Room-Temperature Spin Light-Emitting Diode. *Science* **2021**, *371* (6534), 1129−1133.

(27) Balandin, A. A.; Kargar, F.; Salguero, T. T.; Lake, R. K. One-Dimensional van Der Waals Quantum Materials. *Mater. Today* **2022**, *55*, 74−91.

(28) Kargar, F.; Barani, Z.; Sesing, N. R.; Mai, T. T.; Debnath, T.; Zhang, H.; Liu, Y.; Zhu, Y.; Ghosh, S.; Biacchi, A. J.; Da jornada, F. H.; Bartels, L.; Adel, T.; Hight walker, A. R.; Davydov, A. V.; Salguero, T. T.; Lake, R. K.; Balandin, A. A. Elemental Excitations in MoI$_3$ One-Dimensional van Der Waals Nanowires. *Appl. Phys. Lett.* **2022**, *121* (22), No. 221901.

(29) Cordova, D. L. M.; Chua, K.; Huynh, R. M.; Aoki, T.; Arguilla, M. Q. Anisotropy-Driven Crystallization of Dimensionally Resolved Quasi-1D Van Der Waals Nanostructures. *J. Am. Chem. Soc.* **2023**, *145* (41), 22413−22424.

(30) Island, J. O.; Molina-mendoza, A. J.; Barawi, M.; Biele, R.; Flores, E.; Clamagirand, J. M.; Ares, J. R.; Sánchez, C.; Van der zant, H. S. J.; D'agosta, R.; Ferrer, I. J.; Castellanos-gomez, A. Electronics and Optoelectronics of Quasi-1D Layered Transition Metal Trichalcogenides. *2D Mater.* **2017**, *4*, No. 022003.

(31) Zhu, Y.; Rehn, D. A.; Antoniuk, E. R.; Cheon, G.; Freitas, R.; Krishnapriyan, A.; Reed, E. J. Spectrum of Exfoliable 1D van Der Waals Molecular Wires and Their Electronic Properties. *ACS Nano* **2021**, *15* (6), 9851−9859.

(32) Autès, G.; Isaeva, A.; Moreschini, L.; Johannsen, J. C.; Pisoni, A.; Mori, R.; Zhang, W.; Filatova, T. G.; Kuznetsov, A. N.; Forró, L.; Van den broek, W.; Kim, Y.; Kim, K. S.; Lanzara, A.; Denlinger, J. D.; Rotenberg, E.; Bostwick, A.; Grioni, M.; Yazyev, O. V. A Novel Quasi-One-Dimensional Topological Insulator in Bismuth Iodide β-Bi$_4$I$_4$. *Nat. Mater.* **2016**, *15* (2), 154−158.

(33) Cordova, D. L. M.; Zhou, Y.; Milligan, G. M.; Cheng, L.; Kerr, T.; Ziller, J.; Wu, R.; Arguilla, M. Q. Sensitive Thermochromic Behavior of InSeI, a Highly Anisotropic and Tubular 1D van Der Waals Crystal. *Adv. Mater.* **2024**, No. e2312597.

(34) Milligan, G. M.; Yao, Z.-F.; Cordova, D. L. M.; Tong, B.; Arguilla, M. Q. Single Quasi-1D Chains of Sb$_2$Se$_3$ Encapsulated within Carbon Nanotubes. *Chem. Mater.* **2024**, *36* (2), 730−741.

(35) Farley, K. E.; Shi, Z.; Sambandamurthy, G.; Banerjee, S. Charge Density Waves in Individual Nanoribbons of Orthorhombic-TaS$_3$. *Phys. Chem. Chem. Phys.* **2015**, *17* (28), 18374−18379.

(36) Guo, Z.; Sun, F.; Puggioni, D.; Luo, Y.; Li, X.; Zhou, X.; Chung, D. Y.; Cheng, E.; Li, S.; Rondinelli, J. M.; Yuan, W.; Kanatzidis, M. G. Local Distortions and Metal−Semiconductor−Metal Transition in Quasi-One-Dimensional Nanowire Compounds AV$_3$Q$_3$O$_\delta$ (A = K, Rb, Cs and Q = Se, Te). *Chem. Mater.* **2021**, *33* (7), 2611−2623.

(37) Potel, M.; Chevrel, R.; Sergent, M.; Armici, J. C.; Decroux, M.; Fischer, Ø. New Pseudo-One-Dimensional Metals: M$_2$Mo$_6$Se$_6$ (M = Na, In, K, TI), M$_2$Mo$_6$S$_6$ (M = K, Rb, Cs), M$_2$Mo$_6$Te$_6$ (M = In, TI). *J. Solid State Chem.* **1980**, *35* (2), 286−290.

(38) Hönle, W.; Von schnering, H. G.; Lipka, A.; Yvon, K. New Compounds with Infinite Chains of Face-Condensed Octahedral Mo$_6$ Clusters: InMo$_3$Se$_3$, InMo$_3$Te$_3$, TlMo$_3$Se$_3$ and TlMo$_3$Te$_3$. *J. Less Common Met.* **1980**, *71* (1), 135−145.

(39) Tarascon, J. M.; Hull, G. W.; Disalvo, F. J. A Facile Synthesis of Pseudo One-Monodimensional Ternary Molybdenum Chalcogenides M$_2$Mo$_6$X$_6$ (X = Se, Te; M = Li, Na···Cs). *Mater. Res. Bull.* **1984**, *19* (7), 915−924.

(40) Perryman, J. T.; Velázquez, J. M. Design Principles for Multinary Metal Chalcogenides: Toward Programmable Reactivity in Energy Conversion. *Chem. Mater.* **2021**, *33* (18), 7133−7147.

(41) Perryman, J. T.; Kulkarni, A. R.; Velázquez, J. M. Direct Solid-State Nucleation and Charge-Transport Dynamics of Alkali Metal-Intercalated M$_2$Mo$_6$S$_6$ (M = K, Rb, Cs) Nanorods. *J. Mater. Chem. C* **2020**, *8* (31), 10742−10748.

(42) Ortiz-rodríguez, J. C.; Perryman, J. T.; Velázquez, J. M. Charge Transport Dynamics in Microwave Synthesized One-Dimensional Molybdenum Chalcogenides. *Ind. Eng. Chem. Res.* **2021**, *60* (45), 16153−16161.

(43) Liu, Q.; Zunger, A. Predicted Realization of Cubic Dirac Fermion in Quasi-One-Dimensional Transition-Metal Monochalcogenides. *Phys. Rev. X* **2017**, *7*, No. 021019.

(44) Armici, J. C.; Decroux, M.; Fischer, Ø.; Potel, M.; Chevrel, R.; Sergent, M. A New Pseudo-One-Dimensional Superconductor: Tl$_2$Mo$_6$Se$_6$. *Solid State Commun.* **1980**, *33* (6), 607−611.

(45) Lepetit, R.; Monceau, P.; Potel, M.; Gougeon, P.; Sergent, M. Superconductivity of the Linear Chain Compound Tl$_2$Mo$_6$Se$_6$. *J. Low Temp. Phys.* **1984**, *56* (3), 219−235.

(46) Mori, T.; Yokogawa, Y.; Kobayashi, A.; Sasaki, Y.; Kobayashi, H. Thermoelectricity of Pseudo-One-Dimensional Ternary Chalcogenides: Tl$_2$Mo$_6$Se$_6$ and In$_2$Mo$_6$Se$_6$. *Solid State Commun.* **1984**, *49* (3), 249−252.

(47) Tarascon, J. M.; Disalvo, F. J.; Waszczak, J. V. Physical Properties of Several M$_2$Mo$_6$X$_6$ Compounds (M = Group IA Metal; X = Se, Te). *Solid State Commun.* **1984**, *52* (3), 227−231.

(48) Hor, P. H.; Fan, W. C.; Chou, L. S.; Meng, R. L.; Chu, C. W.; Tarascon, J. M.; Wu, M. K. Study of the Metal-Semiconductor Transition in Rb$_2$Mo$_6$Se$_6$, Rb$_2$Mo$_6$Te$_6$ and Cs$_2$Mo$_6$Te$_6$ under Pressures. *Solid State Commun.* **1985**, *55* (3), 231−235.

(49) Venkataraman, L.; Hong, Y. S.; Kim, P. Electron Transport in a Multichannel One-Dimensional Conductor: Molybdenum Selenide Nanowires. *Phys. Rev. Lett.* **2006**, *96* (7), No. 076601.

(50) Venkataraman, L.; Lieber, C. M. Molybdenum Selenide Molecular Wires as One-Dimensional Conductors. *Phys. Rev. Lett.* **1999**, *83* (25), 5334−5337.

(51) Song, J. H.; Wu, Y.; Messer, B.; Kind, H.; Yang, P. Metal Nanowire Formation Using Mo$_3$Se$_3^-$ as Reducing and Sacrificing Templates. *J. Am. Chem. Soc.* **2001**, *123* (42), 10397−10398.

(52) Messer, B.; Song, J. H.; Huang, M.; Wu, Y.; Kim, F.; Yang, P. Surfactant-Induced Mesoscopic Assemblies of Inorganic Molecular Chains. *Adv. Mater.* **2000**, *12* (20), 1526−1528.

(53) Oh, S.; Chae, S.; Kwon, M.; Ahn, J.; Woo, C.; Choi, K. H.; Jeon, J.; Dong, X.; Kim, T. Y.; Asghar, G.; Kim, H.; Paik, H.; Yu, H. K.; Choi, J.-Y. Organic Dispersion of Mo$_3$Se$_3^-$ Single-Chain Atomic Crystals Using Surface Modification Methods. *ACS Nano* **2022**, *16* (5), 8022−8029.

(54) Wojtera, K.; Walczak, M.; Pietrzak, L.; Fraczyk, J.; Szymanski, L.; Sobczyk-guzenda, A. Synthesis of Functionalized Carbon Nanotubes for Fluorescent Biosensors. *Nanotechnol. Rev.* **2020**, *9* (1), 1237−1244.

(55) Wang, J. Biomolecule-Functionalized Nanowires: From Nanosensors to Nanocarriers. *ChemPhysChem* **2009**, *10* (11), 1748−1755.

(56) Chevrel, R.; Gougeon, P.; Potel, M.; Sergent, M. Ternary Molybdenum Chalcogenides: A Route to New Extended Clusters. *J. Solid State Chem.* **1985**, *57* (1), 25−33.

(57) Sun, L.; Park, S. S.; Sheberla, D.; Dincă, M. Measuring and Reporting Electrical Conductivity in Metal−Organic Frameworks: Cd$_2$(TTFTB) as a Case Study. *J. Am. Chem. Soc.* **2016**, *138* (44), 14772−14782.

(58) Oliveira, F. S.; Cipriano, R. B.; Da silva, F. T.; Romão, E. C.; Dos santos, C. A. M. Simple Analytical Method for Determining Electrical Resistivity and Sheet Resistance Using the van Der Pauw Procedure. *Sci. Rep.* **2020**, *10* (1), No. 16379.

(59) Shen, J.; He, Y.; Wu, J.; Gao, C.; Keyshar, K.; Zhang, X.; Yang, Y.; Ye, M.; Vajtai, R.; Lou, J.; Ajayan, P. M. Liquid Phase Exfoliation of Two-Dimensional Materials by Directly Probing and Matching Surface Tension Components. *Nano Lett.* **2015**, *15* (8), 5449−5454.

(60) Clogston, J. D.; Patri, A. K. Zeta Potential Measurement. In Mcneil, S., Eds.; *Characterization of Nanoparticles Intended for Drug Delivery. Methods in Molecular Biology*; Humana Press: NJ, 2011; Vol. 697, pp. 63−70.

(61) Gannon, L.; Boeri, L.; Howard, C. A.; Gougeon, P.; Gall, P.; Potel, M.; Salloum, D.; Petrović, A. P.; Hoesch, M. Lattice Dynamics of the Cluster Chain Compounds M$_2$Mo$_6$Se$_6$ (M= K, Rb, Cs, In, and Tl). *Phys. Rev. B* **2018**, *98* (1), No. 014104.

(62) Song, J. H.; Messer, B.; Wu, Y.; Kind, H.; Yang, P. MMo$_3$Se$_3$ (M = Li$^+$, Na$^+$, Rb$^+$, Cs$^+$, NMe$_4^+$) Nanowire Formation via Cation Exchange in Organic Solution. *J. Am. Chem. Soc.* **2001**, *123*, 9714.

(63) Xu, Y. C.; Sherman, W. F.; Wilkinson, G. R. A Variable-Temperature Raman Study of Vibrational Modes in NH$_4$I, Suggesting the Existence of a New Low-Temperature Phase. *J. Phys. C: Solid State Phys.* **1987**, *20* (35), L967−L973.

(64) Harvey, K. B.; Mcquaker, N. R. Low Temperature Infrared and Raman Spectra of the Ammonium Halides. *J. Chem. Phys.* **1971**, *55* (9), 4390−4396.

(65) Krishnan, R. S. Raman Spectrum of Ammonium Chloride and Its Variation with Temperature. *Proc. Indian Acad. Sci.* **1947**, *26* (6), 432.

(66) Pigorsch, E. Spectroscopic Characterisation of Cationic Quaternary Ammonium Starches. *Starch - Stärke* **2009**, *61* (3−4), 129−138.

(67) Hashimoto, S.; Tsuda, T.; Ogata, K.; Sugahara, T.; Inoue, Y.; Ohgaki, K. Thermodynamic Properties of Hydrogen + Tetra-n-Butyl Ammonium Bromide Semi-Clathrate Hydrate. *J. Therm.* **2010**, *2010*, 1−5.

(68) De beer, W. H. J.; Heyns, A. M. The i.r. and Raman Spectra of Tetraethylammonium Hexafluoroantimonate (C$_2$H$_5$)$_4$NSbF$_6$. *Spectrochim Acta A* **1981**, *37* (12), 1099−1107.

(69) Young, C. W.; Koehler, J. S.; Mckinney, D. S. Infrared Absorption Spectra of Tetramethyl Compounds. *J. Am. Chem. Soc.* **1947**, *69* (6), 1410−1415.

(70) Zhao, Y.; Xue, M.; Göransson, D. J. O.; Borgström, M. T.; Xu, H. Q.; Chen, J. Probing Strain in Wurtzite InP-InAs Core-Shell Nanowires with Raman Spectroscopy. *Phys. Rev. B* **2021**, *104* (23), No. 235309.

(71) Hyler, F. P.; Wuille bille, B. A.; Ortíz-rodríguez, J. C.; Sanz-matias, A.; Roychoudhury, S.; Perryman, J. T.; Patridge, C. J.; Singstock, N. R.; Musgrave, C. B.; Prendergast, D.; Velázquez, J. M. X-Ray Absorption Spectroscopy Insights on the Structure Anisotropy and Charge Transfer in Chevrel Phase Chalcogenides. *Phys. Chem. Chem. Phys.* **2022**, *24* (28), 17289−17294.

(72) Horrocks, D. L. Techniques for the Study of Excimers; In Horrocks, D. L., Peng, C. T., Eds.; *Organic Scintillators and Scintillation Counting*; Academic: New York, 1971, pp. 75−90.

(73) Kajiwara, T.; Chambers, R. W.; Kearns, D. R. Dimer Spectra of Rhodamine B. *Chem. Phys. Lett.* **1973**, *22* (1), 37−40.

(74) Antonov, L. UV−Vis Spectroscopic and Chemometric Study on the Aggregation of Ionic Dyes in Water. *Talanta* **1999**, *49* (1), 99−106.

(75) Cassidy, J. P.; Tan, J. A.; Wustholz, K. L. Probing the Aggregation and Photodegradation of Rhodamine Dyes on TiO$_2$. *J. Phys. Chem. C* **2017**, *121* (29), 15610−15618.

(76) Radiul, S. M.; Chowdhury, J.; Goswami, A.; Hazarika, S. Fluorescence Spectroscopy Based Characterisation Method for Aggregation Behaviour of Rhodamine B (RhB) in Water, Ethanol, and Propanol. *Laser Phys.* **2022**, *32* (7), No. 075602.

(77) Bujdák, J.; Iyi, N. Molecular Aggregation of Rhodamine Dyes in Dispersions of Layered Silicates: Influence of Dye Molecular Structure and Silicate Properties. *J. Phys. Chem. B* **2006**, *110* (5), 2180−2186.

(78) Sun, L.; Campbell, M. G.; Dincă, M. Electrically Conductive Porous Metal−Organic Frameworks. *Angew. Chem., Int. Ed.* **2016**, *55* (11), 3566−3579.

(79) Olivier, Y.; Niedzialek, D.; Lemaur, V.; Pisula, W.; Müllen, K.; Koldemir, U.; Reynolds, J. R.; Lazzaroni, R.; Cornil, J.; Beljonne, D. 25th Anniversary Article: High-Mobility Hole and Electron Transport Conjugated Polymers: How Structure Defines Function. *Adv. Mater.* **2014**, *26* (14), 2119−2136.

(80) Rivnay, J.; Mannsfeld, S. C. B.; Miller, C. E.; Salleo, A.; Toney, M. F. Quantitative Determination of Organic Semiconductor Microstructure from the Molecular to Device Scale. *Chem. Rev.* **2012**, *112* (10), 5488−5519.

(81) Yao, Z.; Wang, Z.; Wu, H.; Lu, Y.; Li, Q.; Zou, L.; Wang, J.; Pei, J. Ordered Solid-State Microstructures of Conjugated Polymers Arising from Solution-State Aggregation. *Angew. Chem., Int. Ed.* **2020**, *59* (40), 17467−17471.

(82) Tsen, A. W.; Brown, L.; Levendorf, M. P.; Ghahari, F.; Huang, P. Y.; Havener, R. W.; Ruiz-vargas, C. S.; Muller, D. A.; Kim, P.; Park, J. Tailoring Electrical Transport Across Grain Boundaries in Polycrystalline Graphene. *Science* **2012**, *336* (6085), 1143−1146.